

www.advenergymat.de

High-Entropy Surface Complex Stabilized LiCoO₂ Cathode

Xinghua Tan, Yongxin Zhang, Shenyang Xu, Peihua Yang, Tongchao Liu, Dongdong Mao, Jimin Qiu, Zhefeng Chen, Zhaoxia Lu,* Feng Pan,* and Weiguo Chu*

Elevating the charge voltage of LiCoO2 increases the energy density of batteries, which is highly enticing in energy storage implementation ranging from portable electronics to e-vehicles. However, hybrid redox reactions at high voltages facilitate oxygen evolution, electrolyte decomposition and irreversible phase change, and accordingly lead to rapid battery capacity decay. Here significantly improved high-voltage cycling stability of Mg-Al-Eu co-doped LiCoO₂ is demonstrated. It is found that element co-doping induces a near-surface high-entropy zone, including an innately thin disordered rock-salt shell and a dopant segregation surface. The high-entropy complex can effectively suppress oxygen evolution and near-surface structure deconstruction. The phase change reversibility between O3 and H1-3 and thermal stability of the cathode are greatly enhanced as well. As a result, the co-doped LiCoO₂ exhibits a remarkable cycling performance, retaining 86.3% and 72.0% of initial capacity over 800 and 2000 cycles, respectively, with a high cut-off voltage of 4.6 V. The feasible co-doping approach broadens the perspective for the development of stable lithium-ion batteries with high operating voltages.

X. Tan, Y. Zhang, D. Mao, W. Chu Nanofabrication Laboratory CAS Key Laboratory for Nanophotonic Materials and Devices National Center for Nanoscience and Technology Beijing 100190, China

E-mail: wgchu@nanoctr.cn

X. Tan, S. Xu, J. Qiu, Z. Chen, F. Pan School of Advanced Materials

Peking University

Shenzhen Graduate School Shenzhen 518055, China

E-mail: panfeng@pkusz.edu.cn

Y. Zhang, Z. Lu

School of Chemistry and Chemical Engineering

Guangxi University Nanning 530004, China E-mail: xiazhaolu@gxu.edu.cn

The Institute of Technological Sciences MOE Key Laboratory of Hydrodynamic Transients

Wuhan University

Wuhan 430072, China

Chemical Sciences and Engineering Division Argonne National Laboratory

Lemont, IL 60439, USA

The ORCID identification number(s) for the author(s) of this article can be found under https://doi.org/10.1002/aenm.202300147

DOI: 10.1002/aenm.202300147

1. Introduction

Lithium-ion batteries have made great contributions to modern society, facilitating our daily lives in areas such as portable electronics, electric vehicles and stationary energy storage.[1-3] With the increasing of energy consumption, batteries with higher energy densities are urgently needed. Elevating the working voltage of a battery can proportionally increase the capacity and thus the energy density. As a widely used cathode material, LiCoO2 (LCO) can reach more than 220 mAh g^{-1} when charged to 4.6 V.^[4] However, operating at such a high voltage usually leads to a rapid capacity decay.^[5,6] On the one hand, bulk phase transformations, including O3 to H1-3 and H2 to M1 that occur at 4.55 and 4.2 V, respectively, were considered as the main performance hazard.[7-10] But on the other hand, proper surface engineering can help LCO achieve stable performance

without suppressing these phase transformations.[11-13] Thus, the origin of LCO capacity degradation remains indistinct and needs to be carefully unveiled.

Owing to the heavy O_{2n}-Co_{3d} hybridization, the oxygen oxidation (O^{2-} to $O^{\alpha-}$, $0 < \alpha < 2$) contributes capacity at voltages higher than 4.3 V.[14,15] More specifically, the extraction of lithium ions from the LCO leads to the increases of hole density in the O 2p orbital.^[16] Due to the reduced ionic radius and electrostatic force, $O^{\alpha-}$ has higher mobility than O^{2-} , which can move from bulk to the surface and leak on the interface. [17,18] Oxygen evolution from the particle surface leads to a series of cascading effects. First, it can promote electrolyte decomposition and form a thick cathode electrolyte interphase (CEI) layer.[19] Second, irreversible phase transformation can happen, and the layered structure (CoO₂) may transfer to spinel (Co₂O₄) and even rock-salt (CoO). Last but not least, oxygen escape leads to poor mechanical properties of cathode materials and induces lattice collapse, which cause serious performance degradation of LCO at high voltages.^[12,20,21] Accordingly, prevention of oxygen loss from the lattice is considered to be the key in developing high-voltage LCO with long lifetime.

Foreign element doping has been verified to be an effect method to limit the oxygen evolution and improve the stability of LCO.[20,22,23] Intriguingly, in some doping cases, segregation of the alien dopants can be observed on particle surface. [24,25] For examples, a highly soluble Ni and Al can segregate on the

16146480, 2023, 24, Dwnholaded from https://advanced onlinelibrary.wiely.com/oi/01.0102/aem.20230147 by University Town Of Sherazhen, Wiley Online Library on [2011/1025], See the Terms and Conditions (https://onlinelibrary.viely.com/terms-and-conditions) on Wiley Online Library for rules of use; OA article are governed by the applicable Creative Commons

surface of LCO^[20] and LiNi $_{0.94}$ Co $_{0.06}$ O $_2$, ^[26] respectively. These segregations on the surface can form a high-entropy zone with Co and Li^[27] and reconstruct the surface with more stable structures. ^[28] It has been found that the dopants slightly affect the bulk chemistry, but greatly suppress CEI formation and near-surface phase transformation. ^[20,26] Therefore, rational selection and combination of dopants are expected to effectively tailor the surface of LCO for high voltage operation and long-term cycling stability.

Herein, we propose a Mg-Al-Eu co-doping strategy to construct a near-surface high-entropy zone on LCO particles by exploiting the self-segregation of these dopants on the surface. This approach significantly improves the stability of LCO at a high voltage of 4.6 V. A coherent disordered rock-salt layered can be constructed on the surface during the co-doping process, which works as a robust dam for effectively suppressing oxygen evolution. Near-surface segregation of the three dopants forms a buffer zone for the mobile oxidized oxygen. In detail, the substitution of $\rm Mg^{2+}$ and $\rm Eu^{3+}$ for Li^ helps to form a strong CoO–Mg/Co–O–Eu bond, and suppresses the nearby oxygen oxidation due to the electrochemical inactivity of Mg²⁺ and Eu³⁺; The substitution of Al³⁺ to Co³⁺ can greatly improve the stability of lattice oxygen, this may benefit from the fact that the Al-O bond is much stronger than the Co-O bond, and Al3+ does not participate in the oxidation process. The high-entropy Mg-Al-Eu-Co-Li zone promotes a reversible bulk phase transformation of O3 to H1-3 in LCO, and it shows great success in restraining oxygen evolution and CEI formation. This work not only paves the way for developing stable lithium-ion batteries, but also raises fundamental issues about how the LCO cathode evolves and maintains stable during high voltage operation.

2. Results and Discussion

As illustrated in Figure 1a, the Mg-Al-Eu co-doped LCO (LCO-MAE) was synthesized by using a one-pot solid-state process. The high-entropy zone can form spontaneously on the surface. Both LCO and LCO-MAE consist of micrometer particles, and the latter is slightly smaller (Figure S1, Supporting Information). The prepared LCO and LCO-MAE show a hexagonal R3m structure and no impurities were detected (Figure S2, Supporting Information). The Rietveld refinements of XRD patterns are listed in Table S1, Supporting Information. The c lattice parameter of LCO-MAE was 14.0510 Å, a bit higher than that of LCO (14.0470 Å). After co-doping, the occupancy rate of heavy atoms on the Li sites were 0.41% from the refinement, implying that the Li sites are occupied by Mg and Eu ions. LCO-MAE particles were etched from surface to interior for the detection of the corresponding elements, and the X-ray photoelectron spectra (XPS) signals at different etched times are collected in Figure 1b. The Li, Co, and O signal intensities were almost unchanged during the etching process, while the signal intensities of Mg, Al, and Eu gradually decrease to zero during etching. This result reveals that Al, Mg, and Eu are enriched in the surface region, and their doping depth increases sequentially. Similar to LCO-MAE, Al, and Mg signals also show the gradient doping trend in LCO-A and LCO-MA products (Figure S3, Supporting Information).

High-angle annular dark-field scanning transmission electron microscope (HAADF-STEM) was employed for the atomic scale

structural information investigation. Generally, light elements, such as Li and O, cannot be detected in the HAADF mode (Figure 1c). The cobalt atoms are neatly arranged in the LCO, and there is no abnormality at the interface. In the edge zone of LCO-MAE, obvious signals are observed in the Li layers (Figure 1d), which indicates that Mg and Eu ions occupy the Li sites due to the similar ionic radius. Besides, a thin rock-salt layer (≈1.5 nm) is observed on the surface, which is consistent with the highresolution transmission electron microscopy images (HRTEM, Figure S4e, Supporting Information). The rock-salt layer was also observed in LCO-E (Figure S4c, Supporting Information) and LCO-ME (Figure S4d, Supporting Information). This result indicates that LCO with a nanoscale rock-salt surface layer can be constructed by Eu gradient doping. When observing the central zone of LCO-MAE, the signals in the Li sites almost fully vanished (Figure 1e, Supporting Information). These results further confirm that the Mg and Eu ions were enriched in the surface region. Energy dispersive X-ray spectroscopy (EDS) elemental mappings also demonstrate the Mg, Al and Eu dopants tend to segregate to the surface (Figure 1f). A possible reason for the gradient doping of these elements is that they are difficult to penetrate into the large Co₃O₄ precursor (Figure S5a, Supporting Information). To confirm this hypothesis, we synthesize the LCO material with nano Co₃O₄ precursor (LCO-MAE-Co₃O₄-N, Figure S5, Supporting Information). XPS etch results reveal that the distribution of the dopants in LCO-MAE-Co₃O₄-N is more uniform than that of LCO-MAE.

To evaluate the high-voltage stability, the cells were tested with a cut-off voltage of 4.6 V. As presented in Figure 2a, LCO, LCO-MA, and LCO-MAE exhibit a similar charge/discharge curves and the same specific capacity of \approx 217 mAh g⁻¹ at 0.1 C (1 C = 280 mA g^{-1}). Although the phase transition persists after doping (Figure 2b), LCO-MAE shows much higher capacity than that of LCO at high rates (122 mAh g⁻¹ vs 8 mAh g⁻¹ at 20 C), indicating that LCO-MAE could provide excellent power densities (Figure 2c). Furthermore, LCO-MAE demonstrates a prominent stable long-term cycling performance (Figure 2d and Figure S6, Supporting Information), which exhibits capacity retention of 86.3% and 72.0% after 800 and 2000 cycles at 1 C, respectively. In contrast, LCO and LCO-MA remains capacity of 6.4% and 68.7%, respectively, only after 300 cycles. To the best of our knowledge, the cycling stability of LCO-MAE is state-of-the-art among highvoltage layered cathode materials (Table S2, Supporting Information).

To study the reasons for the degradation of the LCO cathode, we compared the typical charge-discharging curves during cycling (Figure 2e–g). The charge/discharge curves of LCO were severely deformed after cycling, while this deformation was partly and totally suppressed in LCO-MA and LCO-MAE, respectively. The H1-3 to O3 phase transition peaks at $\approx\!4.5$ V in dQ/dV profiles were similar at the 2nd cycle for the three cells (Figure S7, Supporting Information), while they vanished in LCO and LCO-MA after 100 and 200 cycles, respectively. Conversely, the H1-3 to O3 phase transition peak at the 300th cycle in LCO-MAE almost overlaps with the 2nd cycle, implying the significantly enhanced phase transition reversibility. Single- and two-element doping of LCO were also conducted (Figure S8, Supporting Information), which reveals the synergistic effect of Mg–Al–Eu three-element doping on electrode stability. In addition, we investigated the

16146840, 2023, 24, Downloaded from https://advancec

onlinelibrary.wiley.com/doi/10.1002/aenm.202300147 by University Town Of Shenzhen, Wiley Online Library on [20/11/2025]. See the Terms

on Wiley Online Library for rules of use; OA articles are governed by the applicable Creative Common

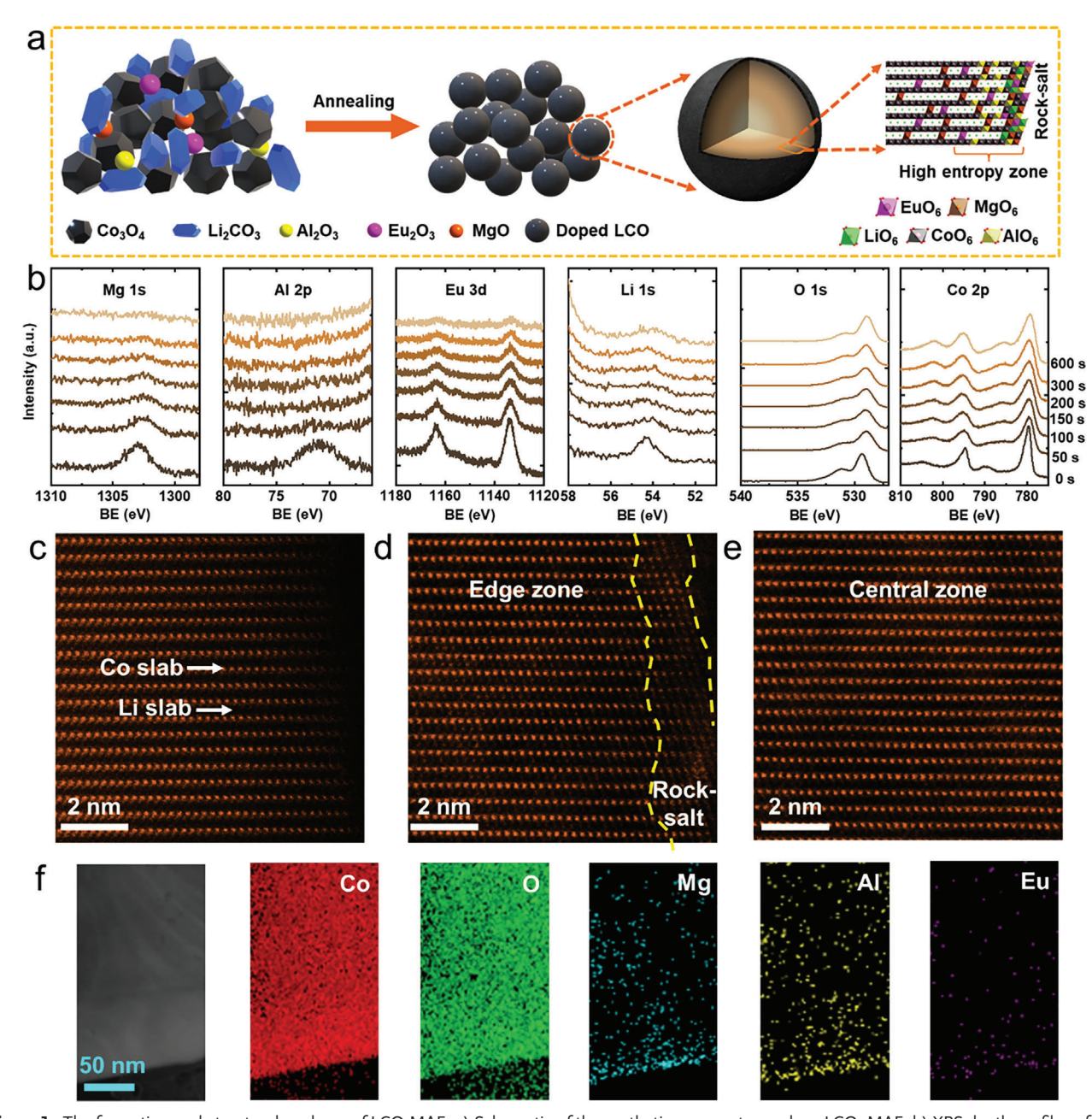


Figure 1. The formation and structural analyses of LCO-MAE. a) Schematic of the synthetic process to produce LCO-MAE. b) XPS depth profiles of Mg 1s, Al 2p, Eu 3d, Li 1s, O 1s, and Co 2p in LCO-MAE. HAADF-STEM images of c) LCO, d) edge zone of LCO-MAE, and e) central zone of LCO-MAE. f) EDS mappings of LCO-MAE.

electrochemical performance of the samples with a doping ratio (LCO-A1.25, LCO-M1.25, and LCO-E1.25) equal to the one for LCO-MAE, the stability of LCO-MAE is obvious better than the others (Figure S9, Supporting Information). More Eu and Mg dopants can permeate into the bulk lattice when increasing the doping ratio, while the cycling performance of LCO-MAE changes little (Figure S10, Supporting Information). Moreover, some other lanthanides (Sm, La, Ce, Pr, Nd) have been verified in the Mg-Al-Ln co-doped LCO (Figure S11, Supporting Information), which validates that such co-doping method is an effective and universal approach to improve the high-voltage cycling stabil-

ity of LCO. It is worth noting that, among the Mg–Al–Ln co-doped LCO, LCO-MAE delivers the best stability. To evaluate the possible expandability of this strategy, we treated Li-rich cathode materials (Li_{1.2}Ni_{0.13}Co_{0.13}Mn_{0.54}O₂) with Mg(NO₃)₂•6H₂O (0.5% molar), Al(NO₃)₃•9H₂O (0.5% molar) and Eu(NO₃)₃•6H₂O (0.25% molar) at 500 °C for 5 h. These dopants also segregate on the surface of secondary particles, and the cycling performance of the product is improved after Mg, Al, Eu co-doping (Figure S12, Supporting Information).

Since the phase transition process may greatly affect the stability of the cathodes, we conducted in-situ XRD measurements

16146840, 2023, 24, Downloaded from https://advanced.onlinelibrary.wiley.com/doi/10.1002/semm.202300147 by University Town Of Shenzhen, Wiley Online Library on [2011/2025]. See the Terms

and Conditions (https://onli

and-conditions) on Wiley Online Library for rules of use; OA articles are governed by the applicable Creative Commons

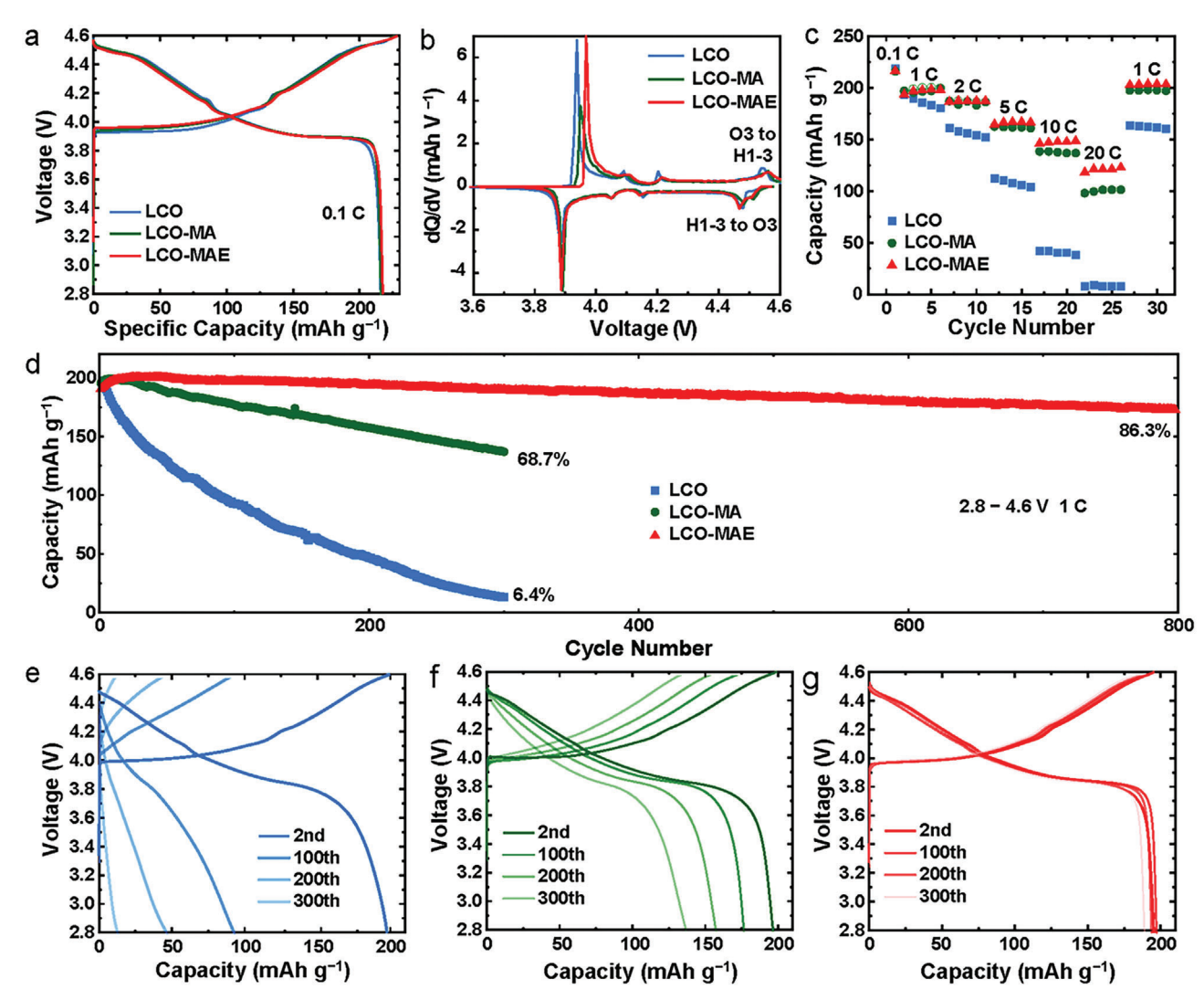


Figure 2. Electrochemical performance of LCO, LCO–MA, and LCO–MAE cells. a) Charge–discharge profiles and b) the corresponding dQ/dV curves. c) Rate capability and d) cycling performance of the cell. Charge–discharge curves of e) LCO, f) LCO—MA, and g) LCO–MAE during cycling at 1 C.

on LCO and LCO-MAE during the first charge-discharge cycle from 2.8 to 4.6 V at 0.1 C (Figure 3 and Figure S13, Supporting Information). The changes of (003) and (110) peaks represent the variation of lattice parameter c and a, [1,24] respectively, and the abrupt (101) and (012) peak change reveals the Co-O slab glide. The (003) peak shift of LCO-MAE was 1.24°, which was a little higher than that of LCO (1.22°). The (110) peak moved in the opposite direction to the (003) peak, but not as sharply, indicating the variation of a was insignificant during the process. The abrupt (101) and (012) peak shift indicates the appearance of the H1-3 phase,[11] and the corresponding structure change is illustrated in Figure 3c. Clearly, the O1a (in H1-3) phase appears at voltage higher than 4.55 V (during charging), which was more intense in LCO-MAE relative to LCO (co-doping of Mg, Al, and Eu fails to suppress the H1-3 phase transformation). Considering the superior high-voltage performance of LCO-MAE, an LCO material with an H1-3 phase during operation can exhibit excellent cycling stability if its near-surface region is stable enough.[11]

To figure out the mechanism of LCO-MAE stability, morphological, and structural evolution of the cells after 300 cycles were investigated in detail, especially in the near-surface regions (Figure 4). The surface of cycled LCO-MAE is smooth, while a rough surface is observed for the cycled LCO (Figure 4a,e), indicating the accumulation of byproducts in the latter.^[29] The rough surface of LCO was further investigated by TEM (Figure 4b). As evidenced by the corresponding selected area electron diffraction (SAED) pattern (Figure 4c) and HRTEM image (Figure 4d), the beneath region was the coexistence of spinel $(Co_3O_4 \text{ or } Li_{1,x}Co_{2+x}O_4)$ and rock-salt (CoO) structures. Similarly, the near-surface region of the cycled LCO-MA degenerated into a spinel structure (Figure S14, Supporting Information). The formation of the above Li-ion blocking phases is accompanied by oxygen releasing, which is inferred from the fact that the ratio of O to Co of these generated structures is lower than that of the pristine layered structure. In contrast, the layered R3m phase and the preformed rock-salt shell were well maintained in LCO-MAE (Figure 4f-h), implying the surface degradation was successfully

16146840, 2023, 24, Downloaded from https://advanced.onlinelbrary.wiley.com/doi/10.1002/kemm.202300147 by University Town Of Shenzhen, Wiley Online Library on [20/11/2025]. See the Terms and Conditions (https://onlinelibrary.wiley

conditions) on Wiley Online Library for rules of use; OA articles are governed by the applicable Creative Common

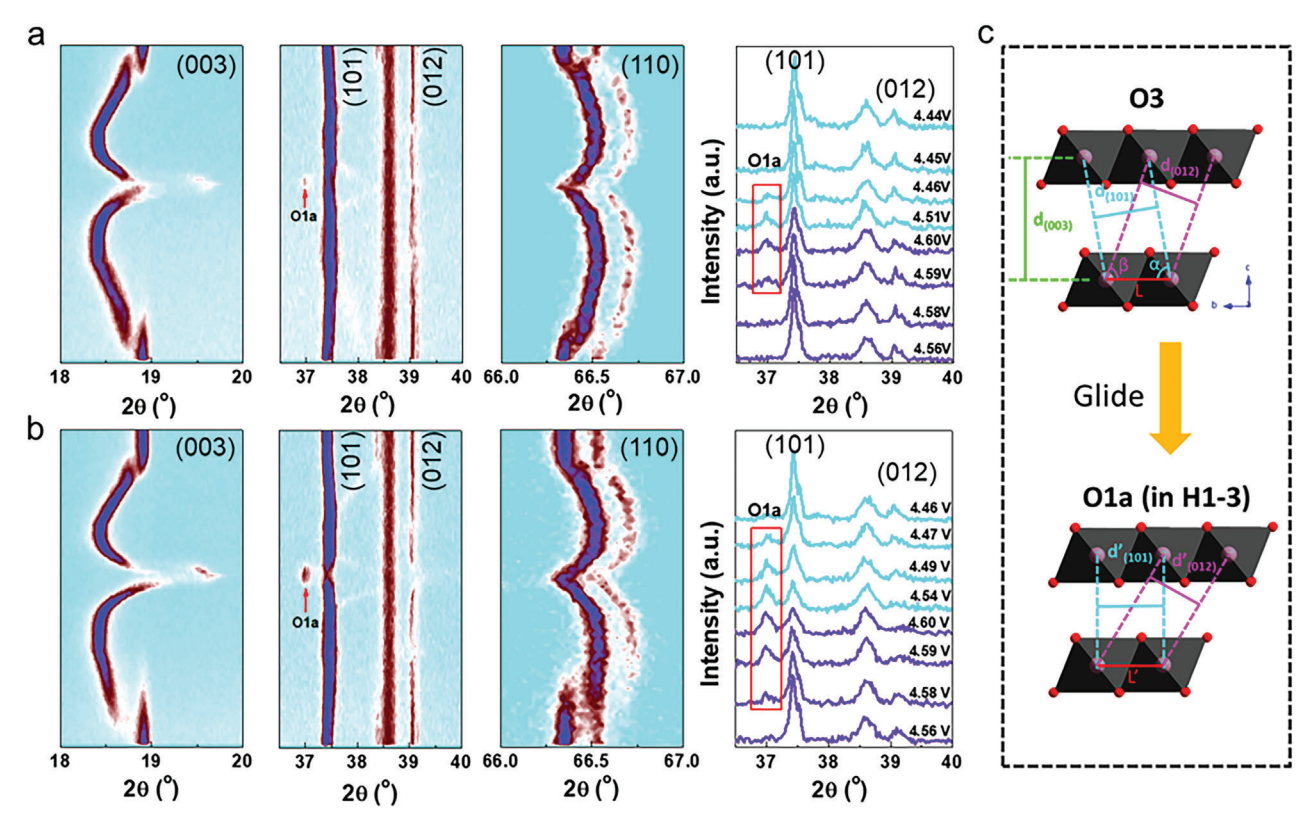


Figure 3. Structural evolution of a) LCO and b) LCO-MAE during the initial charge-discharge process. To elaborate the relationship between O3 and O1a (in H1-3) phase, the stack graphs under the high-voltages are displayed on the right of (a)/(b). c) Schematically illustrate the abrupt $d_{(010)}$ and $d_{(012)}$ change during phase transformation from O3 to O1a (in H1-3); $d_{(101)} = L \times \sin(\alpha)$ and $d_{(012)} = L \times \sin(\beta)$, if the $d_{(003)}$ decrease and no glide happened, $\sin(\alpha)$ and $\sin(\beta)$ will decrease, thus $d_{(101)}$ and $d_{(012)}$ are expected to slightly decrease; However, the $d_{(003)}$ decrease is accompanied by the abrupt increase of $d_{(101)}$ and abrupt decrease of $d_{(012)}$, which implies the glide of the Co–O slab and the phase change from O3 to H1-3.

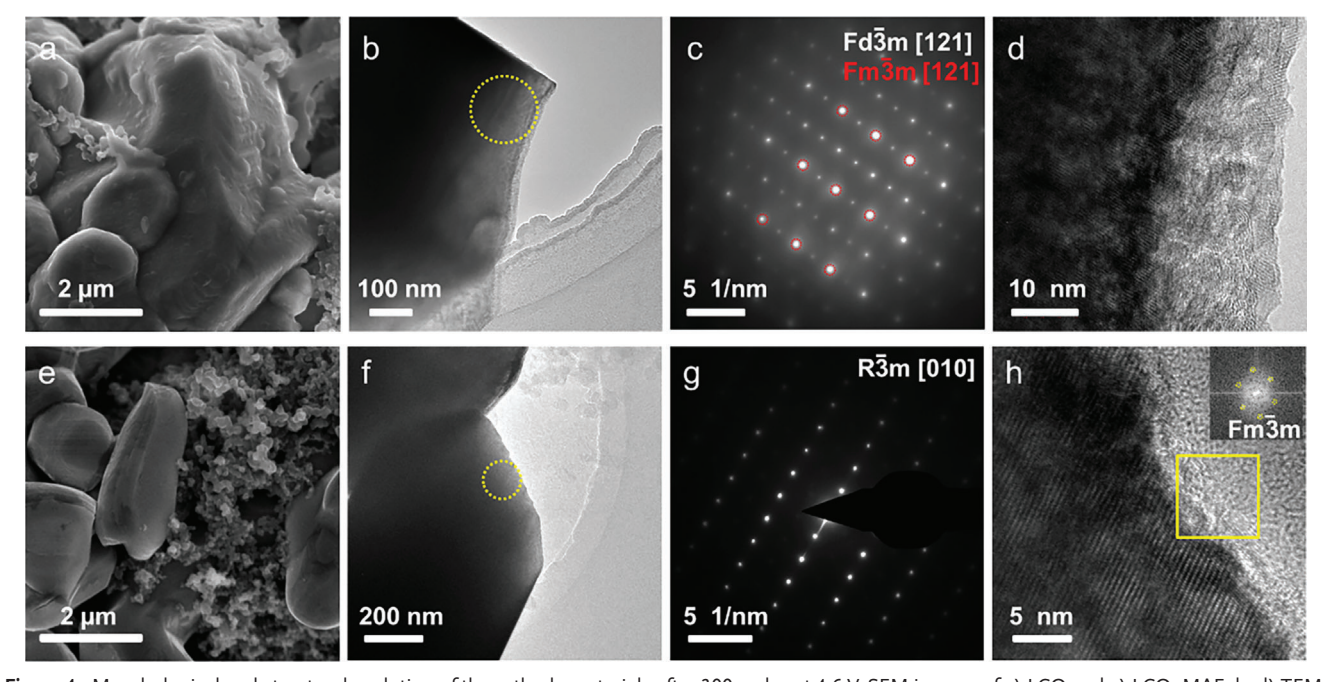


Figure 4. Morphological and structural evolution of the cathode materials after 300 cycles at 4.6 V. SEM images of a) LCO and e) LCO–MAE. b–d) TEM, SAED, and HRTEM images of LCO–MAE. The selected areas for electron diffraction are marked by yellow circles in (b) and (f). The fast Fourier transform region is marked by a yellow square in (h).

16146840, 2023, 24, Downloaded from https://advanced

Lonlinelibrary.wiley.com/doi/10.1002/aenn.202300147 by University Town Of Shenzhen, Wiley Online Library on [2011/2025]. See the Terms and Conditions (https://onlinelibrary.wiley.com/terms-and-conditions) on Wiley Online Library for rules of use; OA articles are governed by the applicable Creative Commons

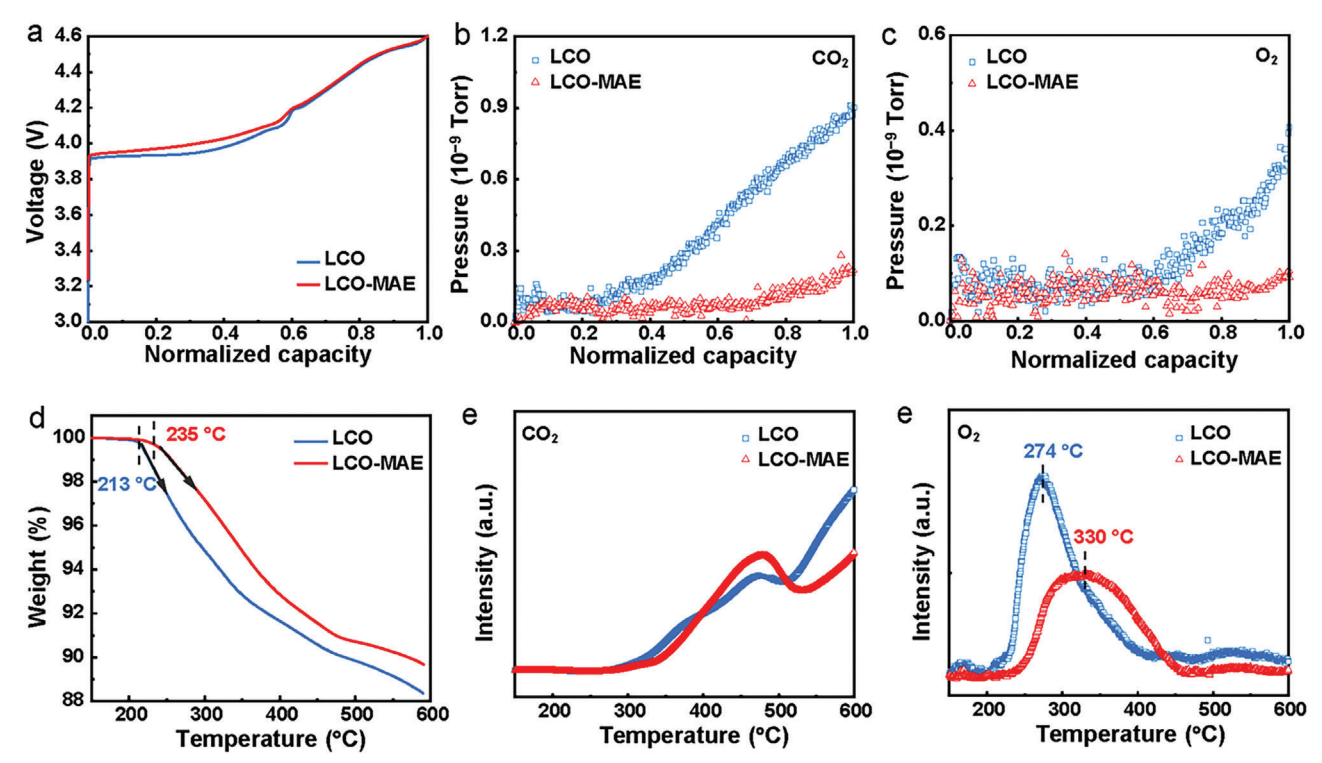


Figure 5. Gas evolution detections during charging and abuse heating. a) In situ DEMS during charge process, and b) CO_2 and c) O_2 release. d) Thermal stability of the charged cathodes, and e) CO_2 and f) O_2 release during abuse heating.

suppressed. Therefore, the high-entropy complex zone can enable excellent stable interfaces during battery operation.

Galvanostatic intermittent titration technique (GITT) was conducted to analyze the role of the near-surface region on lithiumion transport (Figure S15, Supporting Information). The gap between charge/discharge potential and the corresponding relaxation potential is overpotential. The overpotential of LCO increased significantly after 100 cycles, while that of LCO-MAE was almost unchanged during the same process (Figure S15a,b, Supporting Information). Despite the variation of overpotential, the relaxed potentials of LCO at the initial states and after the cycles were similar, implying that capacity decay of LCO is mainly caused by internal impedance increases rather than redox chemistry or thermodynamics changes.^[20] In addition, the calculated lithium-ion diffusion coefficients of LCO-MAE is two orders of magnitude higher than that of LCO in the low voltage range. Electrochemical impedance spectroscopy (EIS) results demonstrate that the charge transfer resistance (R_{ct}) in LCO grew rapidly during cycling, while it was quite stable in LCO-MAE (Figure S16 and Table S3, Supporting Information). The almost unchanged R_{ct} of LCO-MAE indicates that the surface is stable, which is consistent with the TEM results. Cyclic voltammetry (CV) curves show that the stability of LCO at 4.6 V is poor, while the stability of LCO-MAE is quite outstanding, and there is an activation process in LCO-MAE (Figure S17, Supporting Information).

Gas evolution is an important indicator of the stability of the electrodes and electrolyte. [30] To verify the effect of near-surface high-entropy zone on gas evolution at high voltages, in situ differential electrochemical mass spectrometry (DEMS) measurements were conducted during the battery charging (**Figure 5**). An

obvious CO₂ signal was observed in LCO at high voltages (Figure 5b), which is ascribed to the decomposing of the carbonate-electrolyte.^[31] The O₂ signal was clearly detected in LCO at high voltages (Figure 5c), suggesting the loss of lattice oxygen caused by the higher ionic mobility of high-valence O species.^[32] In sharp contrast, there was negligible O₂ and CO₂ evolution in LCO-MAE during the entire charge process. Therefore, Mg–Al–Eu high-entropy interface effectively suppresses the oxygen loss and thereby electrolyte decomposition during battery cycling.

We further clarified the thermal stability by simultaneously probing the weight loss and gas evolution of charged cathodes during abuse heating. As shown in Figure 5d, LCO and LCO-MAE begins to experience obvious weight loss at 213 and 235 °C, respectively. The weight loss rate of LCO is much faster than that of LCO-MAE. The CO₂ (reacted from active material and carbon species) releasing point was delayed in LCO-MAE relative to LCO (Figure 5e). A sharp O₂ peak (274 °C) for LCO and a broad O₂ peak (330 °C) for LCO-MAE were observed (Figure 5f). These results clearly identify that the LCO-MAE exhibits improved thermal stability, which is in consistence with the performance of high entropy Ni-rich layered oxides.^[27] The XRD patterns of the charged LCO and LCO-MAE cathodes after heating at 250 °C for 15 min in argon were displayed in Figure S18, Supporting Information. The Co₃O₄ phase was detected in LCO, while LCO-MAE still exhibited a layered structure, which also means that the thermal stability of LCO-MAE was promoted.

When cycling under high voltages, highly oxidative O_2 and oxygen radicals escaping from the LCO lattice can aggressively decompose the carbonate–electrolyte and form a thick CEI layer.^[33] The cycled electrodes were investigated by time-of-flight

16146840, 2023, 24. Downloaded from https://advanced.onlinelibrary.wiely.com/doi/10.1002/senm.202300147 by University Town Of Shenzhen, Wiley Online Library on [2011/2025]. See the Terms and Condition (https://onlinelibrary.wiely.com/terms-

and-conditions) on Wiley Online Library for rules of use; OA articles are governed by the applicable Creative Commons

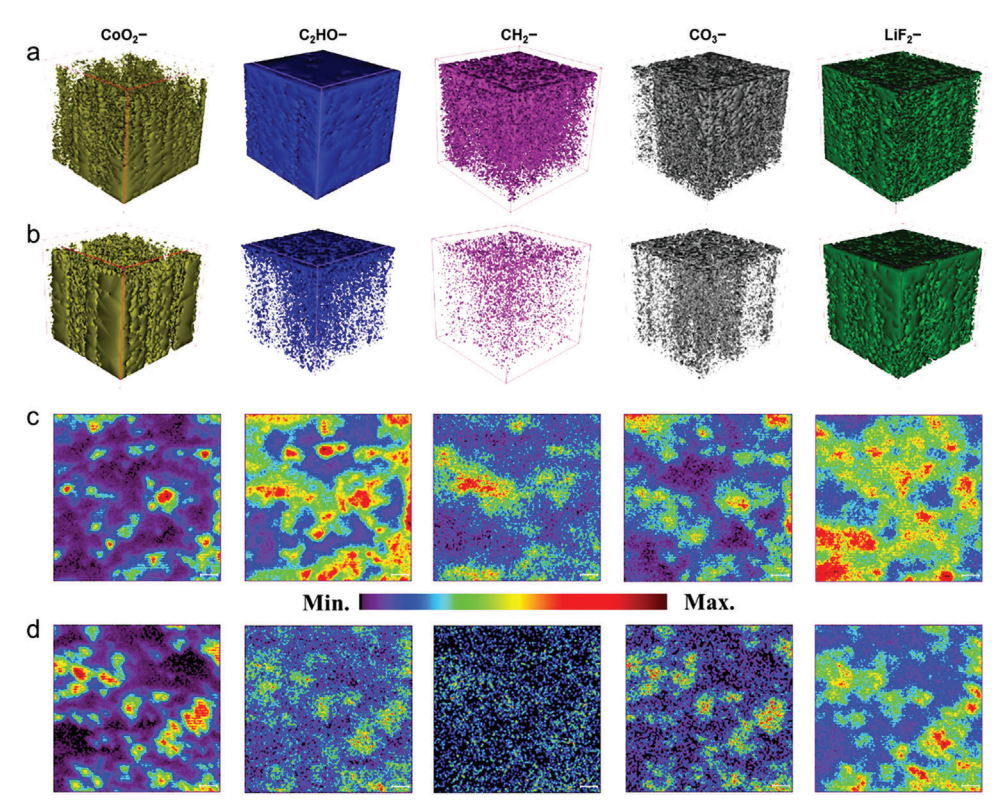


Figure 6. The 3D cathode surface reconstruction. The 3D reconstruction of CoO₂⁻, C₂HO⁻, CH₂⁻, CO₃⁻, and LiF₂⁻ fragments at the a) LCO and b) LCO–MAE cathode surface after 100 cycles. The corresponding vertical TOF-SIMS signals integration of the fragments in c) LCO and d) LCO-MAE.

secondary-ion mass spectrometry (TOF-SIMS) to analyze the information of CEI. The surface of LCO was seriously corroded as its top surface was much rougher than that of LCO-MAE (**Figure 6a**,b). The high content of LiF in LCO–MAE ensures a robust CEI film at high voltages, $^{[21,34,35]}$ which was confirmed by the distribution of the fragments. There was a thicker CEI film in LCO ($\approx\!25$ nm) relative to LCO–MAE ($\approx\!10$ nm) (Figure S19, Supporting Information). The decomposition products of carbonate-electrolytes such as $\rm C_2HO^-$, $\rm CH_2^-$, and $\rm CO_3^-$ species in LCO–MAE are much lower than that of LCO, indicating that the highentropy zone significantly suppressed the carbonate-electrolyte decomposition at high-voltages.

All the CEI species that approximately overlapped with the active material (CoO₂-) of LCO-MAE suggest a stable CEI layer, while the CEI species did not match well with the active material of LCO (Figure 6c). The accumulation of CEI components beyond the zones of active material indicates continuous stripping of CEI layer from LCO during cycling, [36] which implies an unstable and nonuniform CEI film. XPS of the cycled electrodes were presented in Figure S20, Supporting Information. There was more LiF in the cycled LCO-MAE electrode than that of cycled LCO before etching. After 300 s of etching, the signal of Co element in LCO-MAE was stronger than that of LCO, indicating a thicker CEI layer in the latter. The stronger O 1s signal in LCO means that the degree of electrolyte oxidation in LCO is higher than that in LCO-MAE.[20] These results were basically consistent with the TOF-SIMS results. Furthermore, a clear Co signal was detected in the cycled Li anode paired with LCO, but not in LCO-MAE (Figure S20b, Supporting Information), suggesting that Co dissolution was successfully suppressed after Mg, Al, and Eu co-doping.

The suppressed oxygen evolution at high voltage during cycling and the enhanced thermal stability under abused heating of LCO-MAE relative to LCO, is closely related to its near-surface high-entropy zone. To specifically illustrate the stabilization of the high-entropy zone (disordered rock-salt shell and dopantconcentrated layered region), the oxygen-vacancy (V_o) formation energy in the fully de-lithiation layered structure and rock-salt structure are calculated (**Figure 7**). The V_0 formation energy of the plain LCO is 1.954 eV, which increases to 2.075 for the Al doped LCO and over 2.4 eV for the Mg and Eu doped LCO, indicating the enhanced lattice oxygen stability (Figure 7a). Furthermore, the V_o formation energy of the plain CoO rock-salt shell is calculated to be 2.599 eV (Figure 7b), which is higher than that of 1.954 eV for the layered LCO. More importantly, the V_o formation energies increase to 5.049, 4.563, 5.481, and 4.315/5.057 eV in the Al, Mg, Eu, and Li doped CoO rock-salt. These results imply that the high-entropy rock-salt shell can act as a robust dam to suppress the formation and migration of oxygenvacancy, thus considerably improving the structural stability. In brief, the near-surface high-entropy zone prevents the formation of oxygen-vacancy on the interface and let alone migration into the bulk.

3. Conclusion

In summary, we present a Mg–Al–Eu co-doping ${\rm LiCoO_2}$ cathode with significantly improved high-voltage cycling and

OCo,

OAICo,

16146480, 2023, 24, Dwnholaded from https://dwnneed.onlinelibrary.wiely.com/oi/01002/aena.020200147 by University Town Of Sheraben, Wiley Online Library on [2011025], See he Terms and Conditions (https://onlinelibrary.wiely.com/terms-and-conditions) on Wiley Online Library for rules of use; OA articles are governed by the applicable Cerative Commons

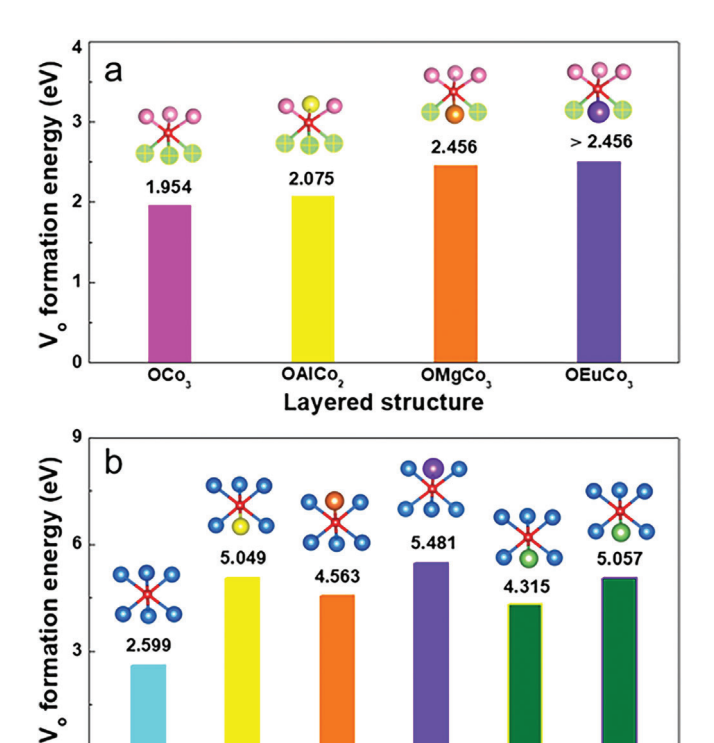


Figure 7. Oxygen-vacancy ($V_{\rm o}$) formation energy at different coordination environments. a) The situation of fully de-lithiation layered LCO. OCo₃ corresponds to undoped LCO, while OAlCo₂, OMgCo₃, and OEuCo₃ correspond to doped LCO. b) The situation of the rock-salt CoO structure. OCo₆ corresponds to undoped CoO, while OAlCo₅, OMgCo₅, OEuCo₅, OLiCo₅ (adjacent to Al), and OLiCo₅ (adjacent to Eu) correspond to doped CoO. It is found that the oxygen vacancy in OEuCo₃ cannot be created since Eu will shift and maintains full coordination with oxygen, thus oxygen-vacancy formation energy in OEuCo₃ is speculated to be higher than 2.456 eV.

OMgCo, OEuCo,

Rock-salt structure

OLICo,

thermal stability. It is found that these dopants are segregated on the surface and form a near-surface high-entropy zone, including a disordered rock-salt shell and a dopant-concentrated region. Such high-entropy region can suppress the oxygen evolution and Co ions dissolution, thereby prevent CEI formation and near-surface structure deconstruction. Aided by the complex surface, the phase change between O3 and H1-3 is highly reversible even after 300 cycles at 4.6 V in LCO–MAE. Consequently, the codoped LCO cathode exhibits a prominent cycling performance with 86.3% capacity retention over 800 cycles at 2.8–4.6 V and 72.0% capacity retention over 2000 cycles at 3.0–4.6 V. These findings shed new light on revealing the stability mechanism of high-voltage layered cathode materials, and advancing batteries with high energy densities for practical applications with feasible approaches.

4. Experimental Section

<code>Materials Synthesis: Bare LiCoO $_2$ and Mg, Al, Eu doped/co-doped LiCoO $_2$ were synthesized by a solid-state reaction approach using Li $_2$ CO $_3$ (98%), Co $_3$ O $_4$ (99.9%), MgO (99%), Al $_2$ O $_3$ (99.9%), and Eu $_2$ O $_3$ (99.99%)</code>

as raw materials. For the preparation of $LiCoO_2$, the Li:Co was 1.05:1 (an excess 5% Li sources was added to compensate for high-temperature lithium loss). For Mg and Al co-doped $LiCoO_2$, the ratio of Li, Co, Mg, and Al was 1.045:0.995:0.005:0.005. For Mg, Al, Ln (Eu, Sm, La, Ce, Pr, Nd) co-doped $LiCoO_2$, the ratio of Li, Co, Mg, Al, and Ln was 1.040:0.995:0.005:0.005:0.0025. The doping ratio of each alien element was the same for all the other samples. The mixed raw materials were calcined at 550 °C for 4 h and then 950 °C for 10 h in air to obtain the products. During the materials formation, Mg and Eu tend to occupy the Li sites while Al occupies the Co site, depending on the size of the atoms.[9,37,38]

Structural and Morphological Characterizations: The morphologies of the samples were examined by scanning electron microscopy (SEM, NOVA NanoSEM 430, Thermo Fisher Scientific, US). The high-resolution TEM images and energy dispersive X-ray spectroscopy (EDS) elemental mapping were acquired on transmission electron microscopy (TEM, Tecnai F20, Thermo Fisher Scientific, US). For atomic structural analysis, the particles were first sliced by focused ion beam (FIB/SEM, Nova200 NanoLab, Thermo Fischer Scientific, USA), and then observed by high-angle annular dark-field scanning transmission electron microscope (HAADF-STEM, JEM-ARM300F, Japan). The powder X-ray diffraction patterns were recorded on an X-ray diffractometer (D/MAX 2500, Rigaku company, Japan) at a step mode (0.02°/step and a sampling time of 1 s). Insitu XRD data were collected using an in-situ XRD cell (Beijing Science Star Technology Co., Ltd, China) at a scanning rate of 5° min-1. The element analysis and etching profiles were acquired on an ESCALab 250Xi electron spectrometer. The element contents of the samples were determined by an ICP-AES (IRIS Intrepid II, Thermo Electron Company, USA). The information of CEI on the cycled cathodes was acquired from timeof-flight secondary-ion mass spectrometry (TOF-SIMS, ULVAC-PHI nanoTOF II, Japan). X-ray photoelectron spectra (XPS) were acquired on an ESCALab 250Xi electron spectrometer (Thermo Fisher Scientific, USA). A simultaneous thermal analyzer coupled with gas chromatography-mass spectrometry (STA-GC/MS, STA8000-Frontier-Clarus SQ8, PerkinElmer, Netherlands) was used for detecting the O₂ and CO₂ evolution and weight loss simultaneously of the charged electrode (SOC: 4.6 V; LCO:PVDF: acetylene black = 94:3:3) during heating (from 30 to 600 °C, 10 °C min⁻¹; N_2).

Electrochemical Measurements: The cathode electrodes were fabricated by mixing LCO (80%), polyvinylidene fluoride (PVDF, 10 wt%), and acetylene black (10 wt%) in N-methyl-2-pyrrolidone (NMP) solvent, followed by casting the slurry onto aluminum foil and dried at 100 °C in a vacuum oven overnight. The mass loadings of active materials in the cathode films were ≈ 2 mg cm⁻². The electrochemical performances were evaluated in CR2025 coin cells with metal Li as anodes, Celgard 2316 as the separator and an electrolyte of 1 $\,\mathrm{M}$ LiPF $_6$ with a 1:1:1 volume ratio of ethylene carbonate: ethyl methyl carbonate: dimethyl carbonate, and 5% vinylene carbonate (VC) additive. The cells were galvanostatic tested at 2.8-4.6 V (1 $C = 280 \text{ mA g}^{-1}$). Cyclic voltammetry (CV) and electrochemical impedance spectroscopy (EIS) measurements were conducted on an electrochemical workstation (CHI660D). Galvanostatic intermittent titration technique (GITT) electrochemical performance measurements were carried out on a Neware battery test system (CT-4008T-5V10mA-164, Shenzhen, China). In situ differential electrochemical mass spectrometry (DEMS) experiment was conducted to detect the O_2 and CO_2 gas evolution during first charge.

Computational Details: DFT calculations were conducted using the Vienna Ab Initio Simulation Package (VASP) with a plane-wave basis set^[39,40] and the projector-augmented wave pseudopotentials.^[41] Generalized gradient approximation (GGA)^[42] in the Perdew–Burke–Ernzerhof (PBE) form was used to treat the exchange-correlation effects.^[43] The plane-wave cutoff energy was fixed at 520 eV. The GGA+U method was used to account for the strong correlation in the calculations.^[44,45] The Hubbard U parameter of Co was 3.3 eV.^[46] The Brillouin zone was sampled by Monkhorst–Pack k-point grid^[47] with a total number of at least 1000/(the number of atoms per cell) points for all directions. The convergence tolerance for residual force was 0.02 eV Å⁻¹ on each atom during structure relaxation. Spin polarization was taken into consideration and the ferromagnetic configuration was set as the initial magnetic structure.

ADVANCED ENERGY MATERIALS 16146840, 2023, 24, Downloaded from https://advanced.onlinelibrary.wiley.com/doi/10.1002/emm.202300147 by University Town Of Shenzhen, Wiley Online Library on [20/11/2025]. See the Terms and Conditions (https://onlinelibrary.wiley.

und-conditions) on Wiley Online Library for rules of use; OA articles are governed by the applicable Creative Commons

To examine the thermodynamic stability of oxygen we calculated the oxygen vacancy formation energy $E_f(V_O)$, which is defined as:

$$E_{f}(V_{O}) = E(V_{O}) + \frac{1}{2}E(O_{2}) - E(pristine)$$
 (1)

where $E(V_O)$ and E(pristine) are the total energy of the oxygen-deficient and pristine structure, respectively. $E(O_2)$ is the energy of an oxygen molecule. To correct the self-interaction errors within DFT, a -1.36eV energy correction for the O_2 molecule was used in all calculations. [46]

Supporting Information

Supporting Information is available from the Wiley Online Library or from the author.

Acknowledgements

X.T., Y.Z., and S.X. contributed equally to this work. This work was financially supported by China Postdoctoral Science Foundation (2022M720207), Strategic Priority Research Program of the Chinese Academy of Sciences (No. XDB36000000), Soft Science Research Project of Guangdong Province (No. 2017B030301013), Shenzhen Science and Technology Research (JCYJ20200109140416788), and Basic and Applied Basic Research Foundation of Guangdong Province (No. 2021B1515130002). This work was also supported from Clean Vehicles, US-China Clean Energy Research Centre (CERC-CVC2) under US DOE EERE Vehicle Technologies Office. Argonne National Laboratory is operated for DOE Office of Science by UChicago Argonne, LLC, under contract number DE-AC02-06CH11357.

Conflict of Interest

The authors declare no conflict of interest.

Data Availability Statement

The data that support the findings of this study are available from the corresponding author upon reasonable request.

Keywords

high-voltage ${\rm LiCoO_2}$, high-entropy complex, Li-ion batteries, Mg-Al-Eu codoping, oxygen evolution

Received: January 15, 2023 Revised: April 13, 2023 Published online: May 4, 2023

- J.-N. Zhang, Q. Li, C. Ouyang, X. Yu, M. Ge, X. Huang, E. Hu, C. Ma,
 S. Li, R. Xiao, W. Yang, Y. Chu, Y. Liu, H. Yu, X.-Q. Yang, X. Huang, L.
 Chen, H. Li, Nat. Energy 2019, 4, 594.
- [2] L. Wang, B. Chen, J. Ma, G. Cui, L. Chen, Chem. Soc. Rev. 2018, 47, 6505.
- [3] W. Li, E. M. Erickson, A. Manthiram, Nat. Energy 2020, 5, 26.
- [4] Y. Lyu, X. Wu, K. Wang, Z. Feng, T. Cheng, Y. Liu, M. Wang, R. Chen, L. Xu, J. Zhou, Y. Lu, B. Guo, Adv. Energy Mater. 2020, 11, 2000982.
- [5] J. Qian, L. Liu, J. Yang, S. Li, X. Wang, H. L. Zhuang, Y. Lu, Nat. Commun. 2018, 9, 4918.

- [6] J. Li, C. Lin, M. Weng, Y. Qiu, P. Chen, K. Yang, W. Huang, Y. Hong, J. Li, M. Zhang, C. Dong, W. Zhao, Z. Xu, X. Wang, K. Xu, J. Sun, F. Pan, Nat. Nanotechnol. 2021, 16, 599.
- [7] T. Tian, T. W. Zhang, Y. C. Yin, Y. H. Tan, Y. H. Song, L. L. Lu, H. B. Yao, Nano Lett. 2020, 20, 677.
- [8] J. Wan, J. Zhu, Y. Xiang, G. Zhong, X. Liu, Y. Li, K. H. L. Zhang, C. Hong, J. Zheng, K. Wang, Y. Yang, J. Energy Chem. 2021, 54, 786.
- [9] Q. Liu, X. Su, D. Lei, Y. Qin, J. Wen, F. Guo, Y. A. Wu, Y. Rong, R. Kou, X. Xiao, F. Aguesse, J. Bareño, Y. Ren, W. Lu, Y. Li, *Nat. Energy* 2018, 3. 936.
- [10] Y. Wang, T. Cheng, Z.-E. Yu, Y. Lyu, B. Guo, J. Alloys Compd. 2020, 842, 155827.
- [11] L. Liu, L. Chen, X. Huang, X.-Q. Yang, W.-S. Yoon, H. S. Lee, J. McBreen, J. Electrochem. Soc. 2004, 151, A1344.
- [12] X. Tan, T. Zhao, L. Song, D. Mao, Y. Zhang, Z. Fan, H. Wang, W. Chu, Adv. Energy Mater. 2022, 12, 2200008.
- [13] A. Yano, N. Taguchi, H. Kanzaki, M. Shikano, H. Sakaebe, J. Electrochem. Soc. 2021, 168, 050517.
- [14] W. S. Yoon, K. B. Kim, M. G. Kim, M. K. Lee, H. J. Shin, J. M. Lee, J. Electrochem. Soc. 2002, 149, A1305.
- [15] W. S. Yoon, K. B. Kim, M. G. Kim, M. K. Lee, H. J. Shin, J. M. Lee, J. S. Lee, C. H. Yo, J. Phys. Chem. B 2002, 106, 2526.
- [16] T. Shang, D. Xiao, F. Meng, X. Rong, A. Gao, T. Lin, Z. Tang, X. Liu, X. Li, Q. Zhang, Y. Wen, R. Xiao, X. Wang, D. Su, Y. S. Hu, H. Li, Q. Yu, Z. Zhang, V. Petricek, L. Wu, L. Gu, J. M. Zuo, Y. Zhu, C. W. Nan, J. Zhu, Nat. Commun. 2022, 13, 5810.
- [17] Z. Zhu, H. Wang, Y. Li, R. Gao, X. Xiao, Q. Yu, C. Wang, I. Waluyo, J. Ding, A. Hunt, J. Li, Adv. Mater. 2020, 32, 2005182.
- [18] Z. Zhu, D. Yu, Z. Shi, R. Gao, X. Xiao, I. Waluyo, M. Ge, Y. Dong, W. Xue, G. Xu, W.-K. Lee, A. Hunt, J. Li, Energy Environ. Sci. 2020, 13, 1865.
- [19] X. D. Zhang, J. L. Shi, J. Y. Liang, Y. X. Yin, J. N. Zhang, X. Q. Yu, Y. G. Guo, Adv. Mater. 2018, 30, 1801751.
- [20] M. Yoon, Y. Dong, Y. Yoo, S. Myeong, J. Hwang, J. Kim, S. H. Choi, J. Sung, S. J. Kang, J. Li, J. Cho, Adv. Funct. Mater. 2019, 30, 1907903.
- [21] Y. Wang, Q. Zhang, Z. C. Xue, L. Yang, J. Wang, F. Meng, Q. Li, H. Pan, J. N. Zhang, Z. Jiang, W. Yang, X. Yu, L. Gu, H. Li, Adv. Energy Mater. 2020, 10, 2001413.
- [22] N. Qin, Q. Gan, Z. Zhuang, Y. Wang, Y. Li, Z. Li, I. Hussain, C. Zeng, G. Liu, Y. Bai, K. Zhang, Z. Lu, Adv. Energy Mater. 2022, 12, 2201549.
- [23] W. Huang, Q. Zhao, M. Zhang, S. Xu, H. Xue, C. Zhu, J. Fang, W. Zhao, G. Ren, R. Qin, Q. Zhao, H. Chen, F. Pan, Adv. Energy Mater. 2022, 12, 2200813.
- [24] L. Wang, J. Ma, C. Wang, X. Yu, R. Liu, F. Jiang, X. Sun, A. Du, X. Zhou, G. Cui, Adv. Sci. 2019, 6, 1900355.
- [25] S. Song, Y. Li, K. Yang, Z. Chen, J. Liu, R. Qi, Z. Li, C. Zuo, W. Zhao, N. Yang, M. Zhang, F. Pan, J. Mater. Chem. A 2021, 9, 5702.
- [26] L. Zou, J. Li, Z. Liu, G. Wang, A. Manthiram, C. Wang, *Nat. Commun.* 2019, 10, 3447.
- [27] R. Zhang, C. Wang, P. Zou, R. Lin, L. Ma, L. Yin, T. Li, W. Xu, H. Jia, Q. Li, S. Sainio, K. Kisslinger, S. E. Trask, S. N. Ehrlich, Y. Yang, A. M. Kiss, M. Ge, B. J. Polzin, S. J. Lee, W. Xu, Y. Ren, H. L. Xin, *Nature* 2022, 610, 67.
- [28] S. Jamil, C. Li, M. Fasehullah, P. Liu, F. Xiao, H. Wang, S. Bao, M. Xu, Energy Storage Mater. 2022, 45, 720.
- [29] A. Fu, J. Lin, Z. Zhang, C. Xu, Y. Zou, C. Liu, P. Yan, D.-Y. Wu, Y. Yang, J. Zheng, ACS Energy Lett. 2022, 7, 1364.
- [30] Y. J. Guo, P. F. Wang, Y. B. Niu, X. D. Zhang, Q. Li, X. Yu, M. Fan, W. P. Chen, Y. Yu, X. Liu, Q. Meng, S. Xin, Y. X. Yin, Y. G. Guo, *Nat. Commun.* 2021, 12, 5267.
- [31] S. Mao, Z. Shen, W. Zhang, Q. Wu, Z. Wang, Y. Lu, Adv. Sci. 2022, 9, e2104841.
- [32] X. Yang, C. Wang, P. Yan, T. Jiao, J. Hao, Y. Jiang, F. Ren, W. Zhang, J. Zheng, Y. Cheng, X. Wang, W. Yang, J. Zhu, S. Pan, M. Lin, L. Zeng, Z. Gong, J. Li, Y. Yang, Adv. Energy Mater. 2022, 12, 2200197.

16146840, 2023, 24, Downloaded from https://advanced.onlinelibrary.wiley.com/doi/10.1002/aemm.202300147 by University Town Of Shenzhen, Wiley Online Library on [20/11/2025]. See the Terms

and Conditions (https://onlinelibrary.wiley.com/term:

and-conditions) on Wiley Online Library for rules of use; OA articles are governed by the applicable Creative Commons

www.advancedsciencenews.com

www.advenergymat.de

- [33] S. Kalluri, M. Yoon, M. Jo, S. Park, S. Myeong, J. Kim, S. X. Dou, Z. Guo, J. Cho, Adv. Energy Mater. 2017, 7, 1601507.
- [34] X. Cao, X. Ren, L. Zou, M. H. Engelhard, W. Huang, H. Wang, B. E. Matthews, H. Lee, C. Niu, B. W. Arey, Y. Cui, C. Wang, J. Xiao, J. Liu, W. Xu, J.-G. Zhang, *Nat. Energy* 2019, 4, 796.
- [35] W. Liu, J. Li, W. Li, H. Xu, C. Zhang, X. Qiu, Nat. Commun. 2020, 11, 3629
- [36] J.-N. Zhang, Q. Li, Y. Wang, J. Zheng, X. Yu, H. Li, Energy Storage Mater. 2018, 14, 1.
- [37] Y. Huang, Y. Zhu, H. Fu, M. Ou, C. Hu, S. Yu, Z. Hu, C. T. Chen, G. Jiang, H. Gu, H. Lin, W. Luo, Y. Huang, Angew. Chem., Int. Ed. 2021, 60, 4682.
- [38] J. Xia, N. Zhang, Y. Yang, X. Chen, X. Wang, F. Pan, J. Yao, Adv. Funct. Mater. 2022, 32, 2212869.

- [39] G. Kresse, J. Furthmiiller, Comput. Mater. Sci. 1996, 6, 15.
- [40] G. Kresse, J. Furthmiiller, Phys. Rev. B 1996, 54, 11169.
- [41] P. E. Blochl, Phys. Rev. B 1994, 50, 17953.
- [42] J. P. Perdew, J. A. Chevary, S. H. Vosko, K. A. Jackson, M. R. Pederson, D. J. Singh, C. Fiolhais, *Phys. Rev. B* **1993**, 48, 4978.
- [43] J. P. Perdew, K. Burke, M. Ernzerhof, Phys. Rev. Lett. 1996, 77, 3865.
- [44] V. I. Anisimov, J. Zaanen, O. K. Andersen, Phys. Rev. B 1991, 44, 943.
- [45] S. L. Dudarev, G. A. Botton, S. Y. Savrasov, C. J. Humphreys, A. P. Sutton, Phys. Rev. B 1998, 57, 1505.
- [46] W. Lei, T. Maxisch, G. Ceder, Phys. Rev. B 2006, 73, 195107.
- [47] H. J. Monkhorst, J. D. Pack, Phys. Rev. B 1976, 13, 5188.